J Mater Sci (2009) 44:4286–4295
DOI 10.1007/s10853-009-3636-z

Control of morphology in inert-gas condensation of metal oxide nanoparticles

Wesley O. Gordon · John R. Morris · Brian M. Tissue

Received: 9 October 2008 / Accepted: 21 May 2009 / Published online: 5 June 2009

Abstract We report preparation conditions to obtain different morphologies of as-deposited refractory metal-oxide nanoparticles using inert-gas condensation with CO_2 laser heating. The micrometer-scale morphology of the nanoparticles depends on the specific metal oxide, the buffer gas composition and pressure, and the target-to-substrate distance. These parameters control the extent to which a plume of nonagglomerated nanoparticles can reach a deposition substrate. Buffer gas pressure has the largest influence for a given material, with lower pressures producing a dense columnar morphology and higher pressures resulting in an open networked morphology. An estimate based on the geometry of the gas-phase plume and experimental results for Y_2O_3 nanoparticles produced in 4 Torr N_2 gives a critical concentration of tens of nanoparticles per μm^3 for the transition of agglomerates versus isolated nanoparticles reaching a deposition substrate.

Introduction

More than two decades of research shows clearly that forming materials at the nanoscale can create new or enhanced structural and physical properties compared to the corresponding macroscale materials [1, 2]. The greatly improved understanding of the preparation and size-dependent properties of isolated nanoparticles makes it easier to begin studying the importance of interparticle arrangement and interactions. Achieving the desired properties of new nanomaterials in applications and devices will often depend on controlling the morphology of the resulting nanostructures in two and three dimensions. For example, the morphology and microstructure of nanoparticles in conjunction with the high surface-to-volume ratio will influence physical properties such as sintering [3, 4], diffusion and adsorption of gases [5], thermal conductivity [6, 7], light absorption, scattering, and manipulation [8–10], and catalytic activity [11–14]. Rechargeable batteries are a prime example of morphology being a determining factor to material performance, where changes after charging/discharging cycles that can lead to device failure [15]. Similarly, a number of applications depend on heterojunctions with their resulting electronic and photonic properties [16], including energy and electron transport [17, 18]. Directed growth or other means of morphology control can be critical to the function of heterojunctions for microelectronic [19] and optical devices [20].

The morphology of nanomaterials during preparation or after modification will also determine their behavior in fluids such as air and water. This behavior will impact their effects in occupational and environmental safety [21, 22], deposition behavior for patterning onto surfaces [23, 24], and their utility as building blocks for new nanocomposites [25]. Controlling morphology during deposition may be especially useful for synthetic advances in device manufacturing. For instance, preparing a nanoparticulate solid with extensive void volume could allow subsequent processing to manufacture a composite material with a high degree of contact between domains. Sophisticated materials preparation in the future will use multiple methods to form complex architectures with unique properties [26].

W. O. Gordon · J. R. Morris · B. M. Tissue (✉)
Department of Chemistry, Virginia Polytechnic Institute and State University, Blacksburg, VA 24061-0212, USA
e-mail: tissue@vt.edu

The active research in the intentional synthesis of nanoparticles has led to a wide variety of methods for creating nanoparticles of most classes of materials [27]. Inert-gas condensation (IGC) is a gas-phase method in which a heat source evaporates source material in a buffer gas to cause nucleation, growth, and sometimes aggregation and/or agglomeration of nanoparticles [28]. In this article, we use "aggregation" to refer to small partly coalesced aggregates and "agglomeration" for larger loosely associated groups of particles. Evaporative techniques allow the use of pressure to control the product material. High-vacuum conditions ($<10^{-4}$ Torr) will produce solid thin films whereas higher pressures (1–100 Torr) can form nanoparticles. When collected on a substrate, nanoparticles will form in very different morphologies compared to films made by low-pressure physical vapor deposition (PVD) [29]. The IGC method has produced nanoparticles of metals [30], metal-oxides [31, 32], semiconductors [33], and hybrid materials [34, 35], and the rapid thermal quench in this process can produce metastable phases that typically exist only under extreme conditions [36, 37]. IGC has also been used to create cm-long filaments of nanoparticles under the influence of an electric field [38].

There are a number of reports of the effects of IGC conditions on the morphology of small particle aggregates [28, 39–42], and several theoretical studies using simple diffusion-controlled [43, 44] and ballistic-deposition models [45] to explain larger-scale morphology. Further theoretical work has studied the influence of particle–particle and particle–substrate interactions [46], thermophoretic dynamics, and particle sintering [47, 48]. Models developed in these studies explain the influence of several parameters on the morphology of the as-deposited nanoparticles, yet they do not fully explain the micrometer-scale morphology of nanoparticles formed by IGC. In our study, we systematically investigate the parameters that influence the deposition and ultimate morphology of refractory nanoparticles after vaporization with a continuous-wave (cw) CO_2 laser. The advantages of this laser-heated method include the wide range of materials that absorb the infrared radiation, the ability to use any buffer gas and gas pressure, and the achievement of the high temperatures necessary to vaporize refractory materials. The gas-phase method also maintains compatibility for direct transfer to high-vacuum systems without exposing material to the ambient atmosphere or solvents for subsequent material processing, analytical characterization, or surface studies [49]. The flexibility of this laser-heated method allows us to study IGC over a broad range of conditions with different gases. Our goal is to determine the relative importance of the experimental parameters that affect nanoparticle formation and agglomeration in cw-laser vaporized materials. We further strive to use our results with models of evaporative processes to understand the resulting morphology of as-deposited nanomaterials. These results will provide predictive information to prepare nanostructures by gas-phase methods regardless of the evaporation source.

Experimental

Figure 1 shows a schematic of the experimental apparatus for synthesizing the nanoparticles in this study [50]. The target rests on a rotatable steel platform in a vacuum chamber. The chamber is evacuated through the pump port via a mechanical pump and can be evacuated to a base pressure of 10^{-6} Torr with a liquid-N_2 trapped oil diffusion pump. Immediately prior to synthesis, the evaporation chamber is isolated from the pumps and purged and backfilled to the desired pressure with the buffer gas. The pressure is measured with a Pirani gauge (Granville-Phillips) using manufacturer-supplied calibration curves. Y_2O_3 targets were made by cold pressing approximately 1 g of powder (Sigma-Aldrich, 99.99%) into a 13-mm diameter pellet, followed by sintering overnight at 1000 °C. ZrO_2 and HfO_2 targets (Cerac, 99.9%) were used as received.

Material is vaporized from the target by focusing a 50 W cw-CO_2 laser (Synrad) beam onto the target to a spot of approximately 1-mm diameter with a 15-cm focal length ZnSe lens. Previous work confirms that this gas-phase condensation method can produce particles of a given size and phase reproducibly [51]. Nanoparticles deposit onto

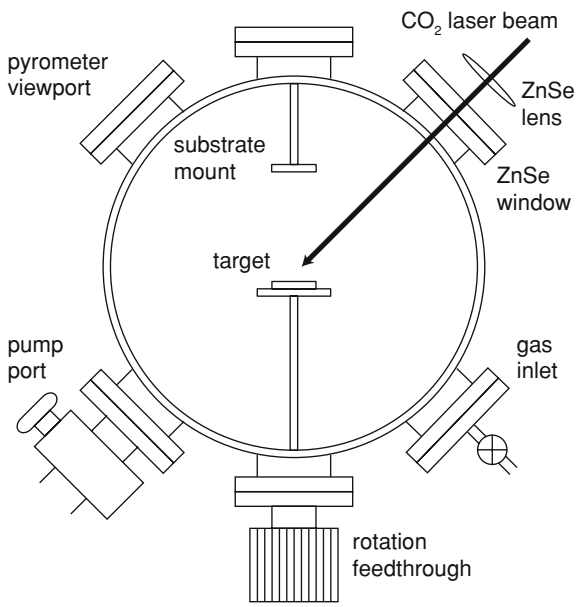

Fig. 1 Schematic of the nanoparticle preparation chamber

substrates that are attached to a support positioned 2.5 cm directly above the target. For microscopy experiments, 4-min evaporations were done onto 1-cm^2 silicon wafer substrates that had been cleaned in piranha solution (conc. H_2SO_4/30% H_2O_2 7:3 by volume), rinsed with copious amounts of deionized water and ethanol, and dried under a stream of ultra-high purity N_2. When collecting larger amounts of nanoparticles for BET measurements and powder X-ray diffraction, the substrate mount was replaced with a cylindrical stainless steel sheet from which nanoparticles were easily scraped. Typical evaporations lasted 30 min or until the target cracked. For high melting point materials such as Y_2O_3, ZrO_2, and HfO_2, deposition rates were approximately 1 mg/min.

Images of as-deposited nanoparticles (sputter coated with Au) were obtained on a LEO 1550 field-emission scanning electron microscope (SEM) with an accelerating voltage of 5 kV. Particle sizes were determined with a Phillips EM 420 scanning transmission electron microscope (STEM) operated at 100 kV. Samples for TEM were prepared by dispersing particles in ethanol and dropping some solution onto a formvar-coated copper grid. High-resolution transmission electron microscopy (HRTEM) images were collected on a Philips CM 300 FEG TEM operating at 297 kV that was equipped with a Gatan GIF 200 electron energy-loss spectrometer and a CCD. To obtain electron-diffraction patterns, several fast Fourier transforms (FFT) of images were averaged using the program Digital Micrograph version 3.5. Atomic force microscopy (AFM) images of ethanol-dispersed nanoparticles on silicon wafers were obtained on a Molecular Imaging PicoPlus AFM operating in tapping mode. X-ray photoelectron spectra (XPS) were obtained with a Perkin Elmer 5400 spectrometer equipped with a Mg(K_α) radiation source. Surface area measurements were performed using the Brunauer-Emmett-Teller (BET) method on a Quantochrome NOVA 1000 analyzer at 77 K. For these measurements, 20 mg of nanoparticles were collected and placed in a quartz tube and degassed under vacuum at 250 °C overnight. Powder X-ray diffraction patterns of nanoparticle powders were obtained on a PANalytical Xpert-Pro X-ray diffractometer with CuK_α radiation by placing powders on a quartz slide that was coated with petroleum jelly. Reflection absorption infrared spectra (RAIRS) were obtained by depositing nanoparticles directly onto a clean gold substrate (EMF Corp) and mounting the sample in the beam path of a Bruker IFS 66v/S infrared spectrometer. The spectrometer operates in reflection mode with p-polarized light incident on the sample at a grazing angle of approximately 86°, reflecting from the gold substrate, and detected by a liquid-N_2 cooled mercury–cadmium–telluride (MCT) detector.

Results and discussion

Morphology

Nanoparticles prepared at 1 Torr N_2 have a dense appearance and are powder-like when scraped from a collector plate. The nanoparticles prepared at 10 Torr N_2 appear translucent and break off in light and fluffy flakes when scraped from the collector. The SEM images in Fig. 2 show that the Y_2O_3 nanoparticles produced under the two pressures have distinctly different morphologies. Figure 2a shows that the nanoparticles prepared under 1 Torr N_2 consist of dense structures of nanoparticles that are columnar with diameters of 1–10 μm. The size of the columnar feature varies with preparation conditions such as vaporization time, gas pressure, and target-to-substrate distance. These column-like features pack in a quasi-hexagonal lattice, and SEM images of "breaks" show that the structure continues through to the substrate (see Fig. 3).

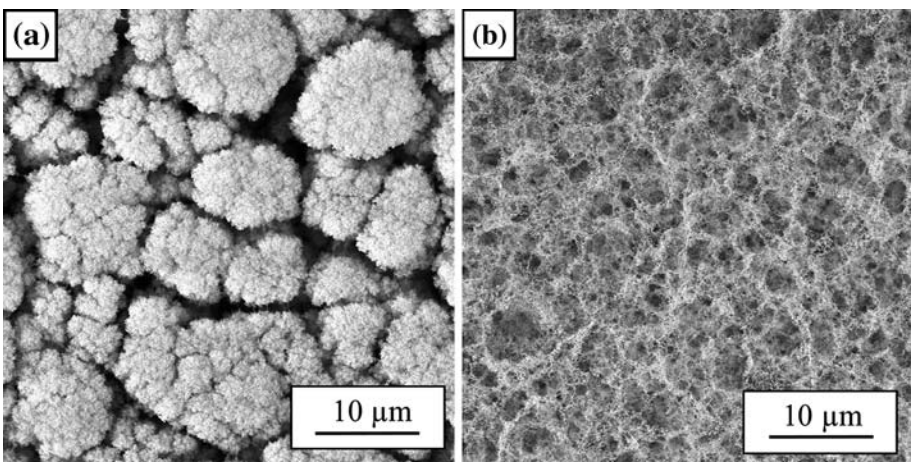

Fig. 2 SEM images of Y_2O_3 nanoparticles made in 1 Torr (**a**) and 10 Torr (**b**) N_2. The magnification is the same for the two images

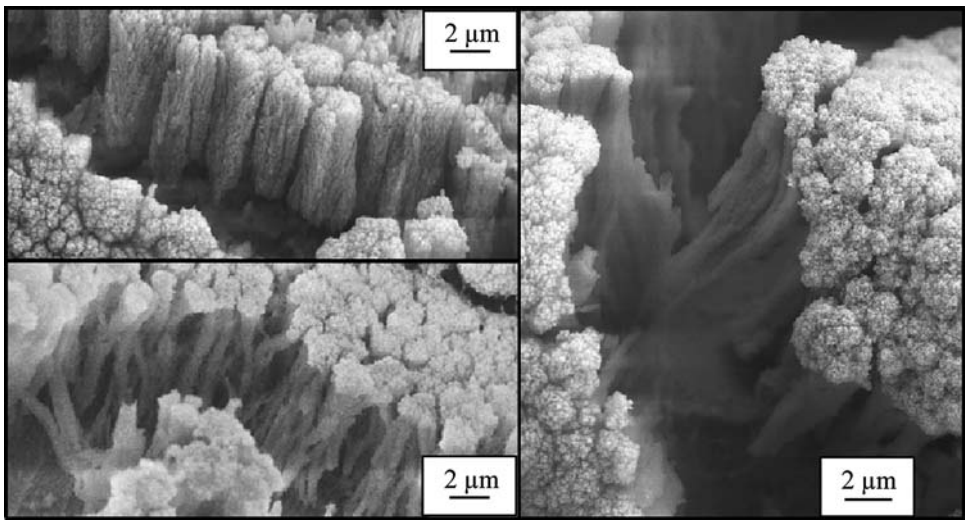

Fig. 3 SEM images of breaks in the film for Y_2O_3 nanoparticle films grown under low pressure showing the column or tree like morphology. The scale bar represents 2 μm in all three images

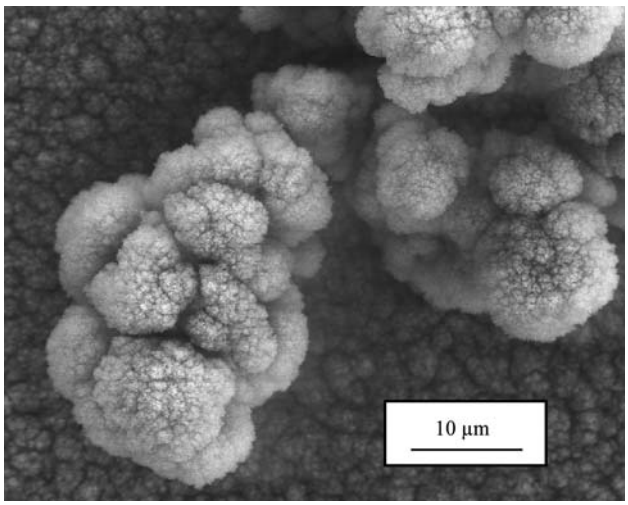

Fig. 4 SEM image of Y_2O_3 nanoparticles produced in 1 Torr N_2 and covering a foreign object (probably a fiber). The nonplanar nature of the "substrate" leads to radial expansion of the columnar structures

We believe that the morphology of these cw-laser-evaporated nanoparticles are the same as for previously reported "columnar structure" of Si nanostructures [52] and the "cauliflower-like structure" of SnO_2 films [53] prepared by pulsed laser deposition (PLD).

Positioning the deposition substrate in different orientations relative to the target shows that columns grow perpendicular to the surface regardless of the substrate orientation. This substrate-directed growth is seen in Fig. 4, where nanoparticles have deposited on a foreign object (perhaps a fiber). The nonplanar nature of the object leads to the particle structures radiating from the surface rather than forming the packed columns seen on the flat substrate. This aspect of the Y_2O_3 nanoparticle growth is not unlike the radiating characteristics of crystalline ZnO nano-nails prepared by thermal evaporation and condensation [54]. This perpendicular growth also shows that the morphology that forms during IGC occurs differently from that of dense films prepared at low pressure or by glancing angle deposition (GLAD) [55], although the columnar structures can be similar in appearance.

Nanoparticles made at higher pressures (10 Torr N_2 and higher, see Fig. 2b) appear to form networked threads of nanoparticles that continue to micrometer lengths with a considerable amount of void space. No evidence was found to suggest that the packing and morphology below the surface is different from what is seen in Fig. 2b. This networked morphology can occur when agglomerates of particles form in the gas phase before depositing on the substrate surface [56]. Agglomerate formation is common when concentrations and residence times of particles are sufficient for diffusion-limited aggregation to occur and when the thermal energy is low enough that the particles do not coalesce on collision. Such conditions are not unique to IGC and "open" morphologies are reported for other evaporative, laser-ablation, and flame preparation methods [39, 42, 57–59]. Comparing the extended network of the Y_2O_3 nanoparticles to simulated agglomerates suggests that at least some of the agglomerates form by cluster–cluster collisions, leading to a fractal dimension of approximately 2 (see Fig. 8.3 in [54]). The appearance is distinctly different from nanoparticle aggregates that form in higher temperature environments [41].

Particle size and crystal phases

Samples of particles produced in 1 and 10 Torr of N_2 were characterized to determine particle size, crystal structure, and surface chemistry. AFM and STEM measurements of dispersed particles show that the mean diameters for Y_2O_3 nanoparticles are 2.5 ± 1.0 and 5.0 ± 0.5 nm for 1 and

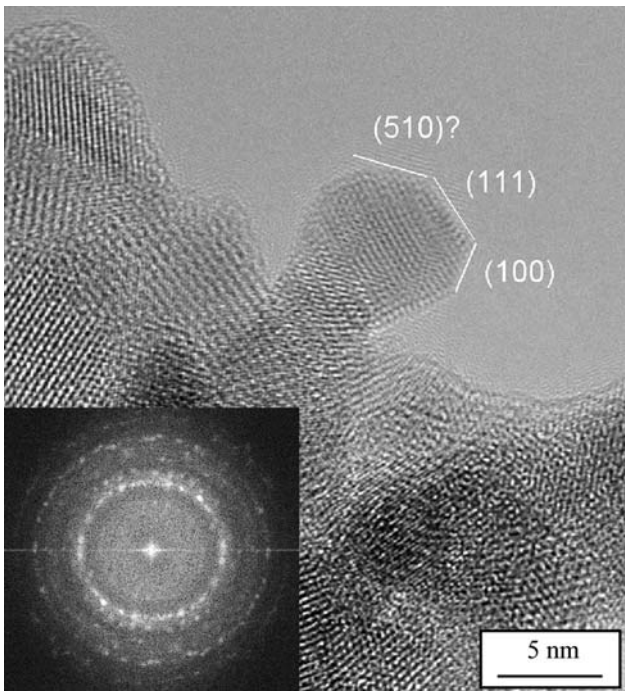

Fig. 5 Typical HRTEM image of Y_2O_3 nanoparticles. Note the substantial aggregation in the sample. Particles synthesized under the different pressures showed no difference other than the degree of agglomeration and particle size. The inset shows an average of the fast Fourier transform of images, revealing a scattering pattern that matches the cubic phase of Y_2O_3

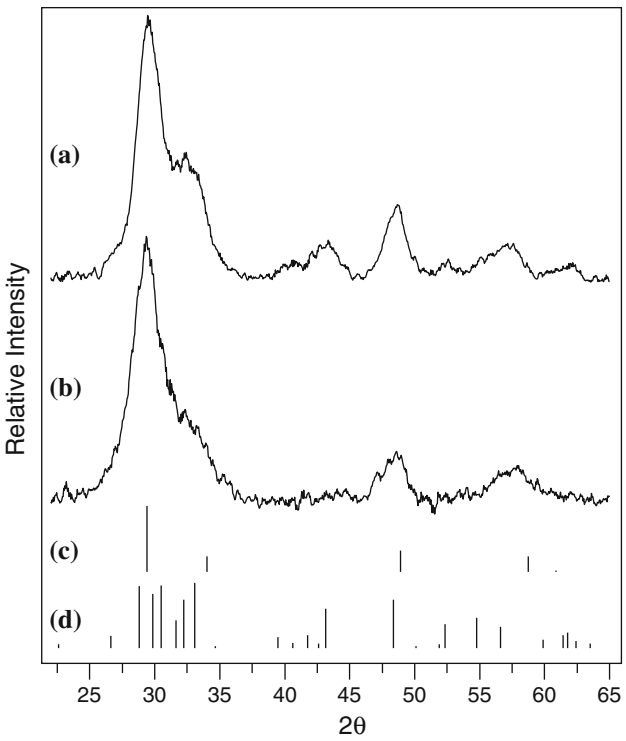

Fig. 6 Powder XRD spectra of nanoparticles produced at (a) 10 and (b) 1 Torr. Reference XRD spectra are shown for the (c) cubic [61] and (d) monoclinic [62] phase of Y_2O_3. The larger particles made at 10 Torr show a greater fraction of particles with the monoclinic phase

10 Torr, respectively. These sizes are consistent with the dependence of particle size on pressure reported previously [51]. HRTEM measurements show that the truncated, cube-shaped particles produced under both pressures have a high degree of crystallinity. Electron-diffraction measurements (shown in the inset of Fig. 5) indicate a cubic (Mn_2O_3-type) crystal structure for the particles [60]. Powder X-ray diffraction measurements (see Fig. 6) reveal that the particles are mostly cubic phase (JCPDS file 44-399) [61], with a small amount of monoclinic phase material also present (JCPDS file 43-661) [62]. Fitting the diffraction data shows that >95% of the smaller particles (formed in 1 Torr N_2) have the cubic phase, while >70% of the larger particles (formed in 10 Torr N_2) are cubic. Using the Scherrer equation for the predominantly cubic reflection at $2\theta = 29.15°$, the crystallite size was estimated to be 2.4 and 3.6 nm for the particles made at 1 and 10 Torr, respectively. The value calculated for the 10 Torr sample is probably an underestimate due to the broadening of the line due to the overlapping monoclinic phase reflections (see Fig. 6). Since nanoparticles for the powder XRD are collected over a slightly larger range of target-to-substrate distances compared to the more localized collection onto the silicon substrates, some difference is expected and these values are consistent with the microscopy results.

XPS and RAIRS show that the nanoparticles are free of inorganic contaminants, but they do have a substantial amount of surface carbonate groups. Presumably adsorbed carbon dioxide degasses when the target is heated with the laser. BET analysis determined the specific surface areas of the nanoparticles to be 187 and 155 m^2/g for synthesis in 1 and 10 Torr N_2, respectively. Comparing these numbers with calculations based on the mean size for spherical particles, 60% of the surface area is obscured by grain boundaries with neighboring particles for the nanoparticles formed at 1 Torr and 39% for the nanoparticles grown at 10 Torr. The higher fraction of surface area masked by particle boundaries or inaccessible pores for the 1 Torr N_2 sample is consistent with the higher particle density seen in the SEM images. Table 1 summarizes the nanoparticle characteristics determined from these experiments.

Deposition mechanism

Several experiments were performed to explore the deposition mechanism of the nanoparticles onto the substrate:

Table 1 Summary of Y_2O_3 nanoparticles prepared at "low" and "high" buffer gas pressures

	Low pressure (1 Torr N_2)	High pressure (10 Torr N_2)
Bulk morphology on scraping	Particulate and adherent	Flaky and loose
SEM morphology	Columnar	Networked threads
Size (from AFM and STEM)	2.5 ± 1.0 nm	5.0 ± 0.5 nm
Phase (cubic:monoclinic)	>95:5	>70:30
BET surface area	187 m^2/g	155 m^2/g
Calculated inaccessible surface	60%	39%

- determining morphology as a function of target-to-substrate distance,
- testing for postdeposition particle diffusion with a cooled substrate, and
- electron microscopy after short vaporization times to monitor initial deposition.

The distance between the target pellet and the substrate was varied from 0.5 to 8 cm for both 1 and 10 Torr N_2 atmospheres. No significant distance dependence was observed in the morphology of these nanoparticles. These results indicate that nucleation and rapid initial growth of the nanoparticles occur very close to the target. Since the number of nucleation sites in the gas phase is not known, the relative contributions to particle growth by vapor-phase growth versus coalescence of primary particles is also unknown. However, achieving similar morphology at 0.5 and 8 cm suggests that little coalescence occurs for refractory materials at 0.5 cm from the target, which is not necessarily true for materials with much lower melting points [63]. Although vapor-phase growth can continue throughout the chamber volume, the concentration of the source material in the gas phase is depleted rapidly and we believe that addition of monomers to the nanoparticles far from the target has a small relative effect on their size. Preparing nanoparticles at different N_2 buffer gas pressures between 1 and 10 Torr for the 8 cm target-to-substrate distance showed a transition between the "low" and "high" pressure morphologies (refer to Fig. 2) at approximately 3 Torr. Repeating the distance-dependence experiment at 4 Torr (slightly above the transition pressure), the morphology changed from the columnar to the networked morphology at approximately 0.9 cm. These 4-Torr experiments show that the substrate-to-target distance can affect the resulting morphology, but that distance has much less influence than the buffer gas pressure. Since gas-phase concentrations of nanoparticles are higher closer to the target, this experiment also suggests that some mechanism prevents agglomeration before reaching a certain distance from the target. We hypothesize that sufficient cooling is necessary for agglomeration, but we cannot rule out that the nanoparticles are charged and repel each other electrostatically. Although a transition from coalescence to agglomeration could also explain this distance dependence, we do not observe ramified aggregates for these refractory nanoparticles that would be expected in such a case [64].

To test for the occurrence of particle diffusion after deposition, nanoparticles were grown in 1 Torr of N_2 with the substrate at ambient temperature and at approximately 100 K. Both samples exhibited the columnar morphology with no apparent restructuring. This "locking in" of the particle morphology is attributed to the refractory nature of Y_2O_3. One obvious difference in the samples was the presence of cracks in the nanoparticle "film" that formed on the low temperature substrate, presumably due to expansion when warmed. These cracks were approximately 10 μm wide and 100–300 μm long, compared to the 2–5 μm spaces observed between the columns. Since cooling is more rapid at higher buffer gas pressure, no restructuring is expected for nanoparticles formed at higher pressure.

Initial development of the as-deposited morphology was investigated by collecting SEM images of nanoparticles formed in 1 and 10 Torr N_2 after 5 s of vaporization. Figure 7 shows that nanoparticles made in 1 Torr N_2 form much smaller initial agglomerates on the surface than those made in 10 Torr N_2. At slightly longer vaporization times, nanoparticles grown at 1 Torr N_2 show small agglomerates covering the surface before the growth of columns begin. This critical surface coverage for columnar growth is on the order of a few layers of small particle agglomerates. This behavior is consistent with that observed for the silicon nanostructures synthesized by Levoska and co-workers, where "soft agglomerates" formed on the surface, followed by development of a regular columnar pattern [52]. Figure 8 shows the development of the as-deposited morphology after 30 s of evaporation. Columns are beginning to grow, but a large amount of free space remains between them. Figure 8 also shows the thin layer of nanoparticles deposited initially, which are visible on the substrate surface between the growing columns. As further deposition occurs, competitive shadowing produces the structures seen in Figs. 2a, 3, and 4. The nanoparticles

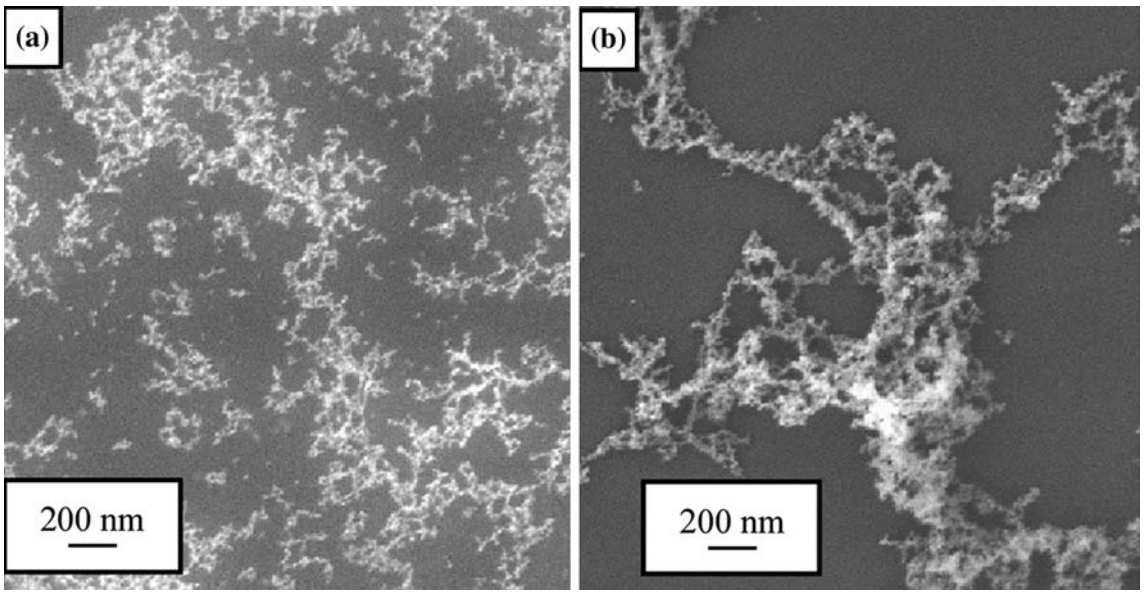

Fig. 7 Comparison of the initial build-up of nanoparticles on the substrate at **a** 10 Torr and **b** 1 Torr. At the higher pressure, agglomerate size is much greater and only a few isolated smaller agglomerates are observed

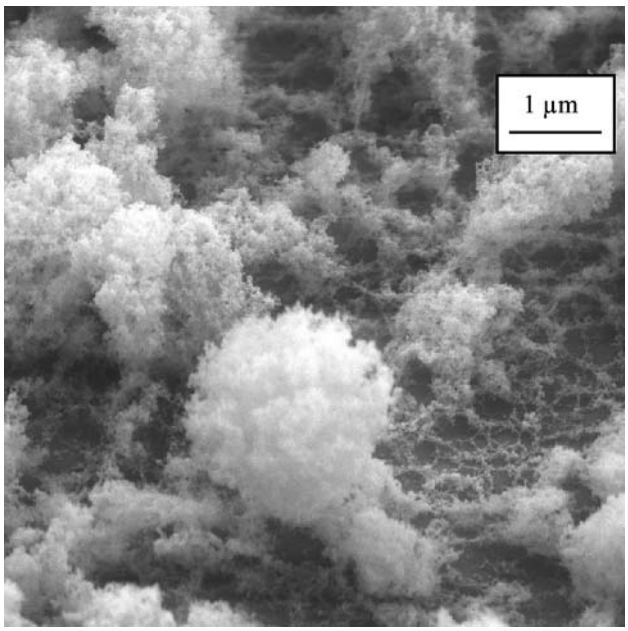

Fig. 8 SEM image taken of film during an early state of growth produced under 1 Torr N_2 after 30 s of vaporization. Image was collected with the substrate at a 45°. Note the layer of small agglomerates on the substrate and the beginning of column growth

that form the networked morphology in 10 Torr N_2 show no difference at low and high coverage. We conclude that the surface morphology seen in Fig. 2b exists throughout the film.

Plume model

It is clear that there is a transition in the deposition mechanism for nanoparticles synthesized at different buffer gas pressures. Similar pressure-dependent transitions from a dense morphology to an open network appear for pulsed-laser deposition of Ga_2O_3 and FeCo [57, 65]. It is established that evaporating a target with a laser within a certain pressure range forms a plume of material [28, 58, 66, 67]. This spatially confined plume is the volume in which nucleation, growth, and limited aggregation of particles can occur. Any extensive agglomeration of particles is taken to occur outside of the plume in an "agglomeration region." The plume shape and plume dynamics such as flow, particle nucleation timescales, and residence times can vary under different conditions [66, 67]. Our results show that the primary factor controlling the morphology of nanoparticles deposited on a substrate in IGC, in the absence of forced convective flow, is the effect of the buffer gas pressure on the plume. A higher buffer gas pressure leads to a radially compressed plume so that the concentration of nanoparticles remains high enough for subsequent agglomeration to occur. A higher pressure also results in a greater degree of Brownian motion [41, 68], and thus a longer residence time for particles to collide and agglomerate prior to deposition. At the higher pressure conditions (>3 Torr N_2 for Y_2O_3 at our laser power), the substrate is located outside of the plume volume and beyond the agglomeration region. Thus, fractal-like agglomerates deposit randomly with little dependence on the substrate, resulting in the web-like morphology and extensive void space.

Conversely, lower pressures (<3 Torr N_2) allow a radially extended plume of individual nanoparticles with a lower number density of nanoparticles in the gas phase. This condition leads to a lower probability of

particle–particle collision and less agglomeration in the gas phase before nanoparticles reach the deposition substrate. Once a critical layer of particles or small agglomerates have accumulated on the surface, short-range forces can influence the deposition of more particles [47], resulting in the column-like structures. During the deposition time, the size of the columns increases while the number density of columns decreases due to preferential growth or competitive shadowing. Particles pack more densely due to the lack of agglomeration prior to encountering the substrate.

The distance determination for agglomeration at 4 Torr N_2 provides data to calculate the nanoparticle density at which agglomeration occurs. We have measured the maximum deposition rate previously to be approximately 1 mg/min for refractory materials at 50 W of laser power. Table 2 lists the concentration density of 3-nm nanoparticles in the gas phase at 10 mm from the target for different plume dimensions. The calculated values assume equal amounts of material transiting through each of 100 slices of a 100-mm high cone above the target. The values in Table 2 are nanoparticle concentrations in the last slice, i.e., between 99 and 100 mm from the target, prior to agglomeration. The mass of material is assumed to be distributed uniformly in the gas phase with no residual yttria monomer and a total transit time of 0.1 s between the target and substrate [69]. The density of Y_2O_3 is taken to be the bulk value of 5.1 g/cm^3. Our experiment conditions are estimated to be a 45° cone angle and 0.5 mg/min deposition rate, leading to a concentration of 15 nanoparticles per μm^3 for the onset of agglomeration. Doing a similar calculation for material radiating from the hot spot in all directions above the target, i.e., a hemisphere, gives a nanoparticle density nearly an order of magnitude less than for the cone (1.9 μm^{-3} for a 0.5 mg/min deposition rate).

Given the uncertainty in the assumptions, these results are merely order of magnitude estimates. However, they provide some guidance in predicting the onset of agglomeration and they correlate well with the characteristic distance for Brownian motion of 50 μm calculated for 3-nm diameter Y_2O_3 particles in 4 Torr of nitrogen. This calculation of the particle length scale, l_{pa}, assumes the free molecule range for l_{pa} much larger than the mean free path of the surrounding gas [56]. This calculation makes the same assumptions as above and estimates the temperature 10 mm from the target to be approximately 1000 K [69, 70]. Even if the temperature is much lower, the particle path length scale is still on the order of 10 μm.

Table 2 Approximate concentrations of 3-nm nanoparticles in the gas phase 10 mm from the target

Cone angle	Dia:height ratio	Density of 3-nm diameter nanoparticles, μm^{-3}		
		1.0 mg/min	0.5 mg/min	0.1 mg/min
20	0.364	224	112	22
25	0.466	137	68	14
30	0.577	89	45	8.9
35	0.700	61	30	6.1
40	0.839	42	21	4.2
45	1.000	30	15	3.0
50	1.192	21	10	2.1
55	1.428	15	7.3	1.5
60	1.732	9.9	5.0	1

Buffer gas dependence

To gain some predictive insight into the deposition process and the resulting morphology, we determined the transition pressure for the change from columnar to networked morphology for different buffer gases. Table 3 lists the gases and the approximate pressure at which the morphology changes based on SEM images.

Although we know that yttria nanoparticles have carbonate on the surface, there is no apparent difference in the resulting morphology when using the CO_2 atmosphere. The dependence on buffer gas is fairly slight. Although the vaporization mechanism is different, we expect the plume in cw-laser evaporation to behave similar to the laser-ablated plume in PLD, for which heavier gases confine the plume more than do lighter gases [71]. With the exception of krypton, the transition pressure for most of the other gases in Table 3 showed predictable behavior. The transition pressure for argon is slightly lower than expected for its mass, but the observed transition pressure is not far from the other gases given that the uncertainty in the experiment is estimated to be ±1 Torr. Helium has a higher transition pressure than the other gases, although the exact value was undetermined since it was beyond the calibration range of our pressure measurement. Similar results have been observed for PLD in helium atmosphere due to this light gas not being able to confine the plume appreciably [72].

Table 3 Approximate transition pressure for different buffer gases at which Y_2O_3 nanoparticles change from the columnar (lower pressure) to the networked (higher pressure) morphology

Gas	Formula weight, g/mol	Transition pressure, Torr
He	4.00	>10
Ne	20.18	4
N_2	28.01	3
O_2	32.00	4
Ar	39.95	0.8
CO_2	44.00	3
Kr	83.80	10

The 10 Torr transition pressure for krypton is a clear outlier in our results. It is much higher than expected since this heavy gas is expected to keep the plume compressed. Experiments comparing the "laminar–turbulent transition" for He, Ar, and Kr showed anomalous behavior for Kr [73]. It is possible that Kr is more prone to convection than the other gases, and thus permits a more extended plume than the other gases.

Overall the gas-dependence results are consistent with other work in the literature, especially for the fast plume dynamics with a He buffer gas. Geohegan et al. performed in situ time-resolved spectroscopy of gas-phase synthesized particles and found different plume dynamics for SiO_x nanoparticles produced in 1 Torr Ar and 10 Torr He [66]. Nakata and co-workers used in situ time-resolved spectroscopy to study the effect of gas on the plume dynamics and observed the onset of Si clustering to be fastest in He [67]. Similarly, small metal clusters could be formed in He and detected by mass spectrometry, but not in other gases for which the clusters grew too large [74]. Sánchez-López and co-workers found the smallest ZnS nanoparticles synthesized in He as expected, but nanoparticle size was larger in N_2 than in Ar [42]. To summarize the gas dependence, fast plume dynamics in He leads to smaller nanoparticles and faster transit time to a deposition substrate. Heavier gases will compress a plume to a greater extent, although it is not straightforward to predict plume behavior for all gases as "individual molecular properties" can influence the thermal and physical properties of the buffer gas [75].

Conclusions

The morphology of nanoparticles prepared by IGC can be controlled by varying the type and pressure of buffer gas and, to a lesser extent, the distance between the evaporation source and the deposition substrate. For our conditions, nucleation and growth of the nanoparticles occur very close to the target with little subsequent growth beyond 5 mm. The buffer gas pressure has the greatest influence on morphology by controlling the extent to which a plume of evaporating material is compressed spatially. Higher gas pressures compress the plume and extend the nanoparticle residence time, thereby allowing particle agglomeration in the gas phase. Subsequent deposition results in an open morphology of networked threads that can extend to micrometer lengths. A lower gas pressure allows individual nanoparticles to reach the deposition substrate and form a characteristic columnar structure. For deposition on a substrate at ambient temperature, there is no evidence for restructuring of the nanoparticles after deposition.

Most buffer gases produced similar results for nanoparticle formation and subsequent agglomeration, but the dependence on gas composition was not completely predictable. Helium, due to its low mass, allows the most extended plumes and the fastest transit times. We predict He to be the best buffer gas when trying to achieve the smallest particle size with the least gas-phase agglomeration at high deposition rates. Kr showed unexpected behavior for the onset of nanoparticle agglomeration, requiring a higher pressure than expected based on its mass. We attribute this result to Kr compressing the plume less than expected due to greater convection compared to the other gases.

This systematic study of IGC improves the understanding of what happens to nanoparticles between formation and deposition onto a substrate. Previous studies, e.g., refs. [39, 42, 52, 53, 57–59, 65] report particle morphologies similar to those that we observe in Figs. 2, 3, and 8. Our results show that physical conditions, primarily the evaporation rate and plume dimensions, control the gas-phase density of the cooling nanoparticles and ultimately the morphology of the nanoparticles that deposit onto a substrate. This holds true in our study using cw-laser heating of refractory materials and in the thermal and laser ablation sources for the variety of material types in the prior literature reports. The morphology change that we observe for as-deposited Y_2O_3 nanoparticles occurring at 4 Torr of N_2 for a 10-mm target-to-substrate distance leads to a nanoparticle concentration of 15 nanoparticles/μm^3 for the onset of agglomeration. This calculation gives the minimum gas-phase concentration that is necessary for the agglomeration of refractory nanoparticles, e.g., yttria, zirconia, etc., and we expect that this concentration will be necessary regardless of the evaporation source. We expect this prediction to hold for similar gas-phase processes, i.e., with rapid cooling, in the absence of external influences such as electric fields [38] or sintering [76].

Overall, these results serve as guides to select synthesis parameters to obtain desired morphologies of nanoparticles prepared by gas-phase methods with a rapid thermal quench. They further provide a starting point for designing methods to prepare complex nanostructures, which could enable a greater control of structures for the ongoing development of nanomaterials for commercial applications.

Acknowledgements The authors gratefully acknowledge the assistance of Barbara Reisner at James Madison University for the powder XRD data, Kenneth Livi at Johns Hopkins University for the HRTEM data, and Steve McCartney for assistance with microscopy. Funding was provided by the U.S. Army Research Office under Grant W911NF-04-1-0195.

References

1. Fissan H, Kennedy MK, Krinke TJ, Kruis FE (2003) J Nanopart Res 5:299
2. Seifert G (2004) Nat Mater 3:77
3. Bowen P, Carry C (2002) Powder Technol 128:248
4. Groza JR (1999) Nanostruct Mater 12:987
5. Lee TG, Hyun JE (2006) Chemosphere 62:26
6. Kuhlmann SA, Reimann J, Will S (2006) J Aerosol Sci 37:1696
7. Timofeeva EV, Gavrilov AN, McCloskey JM, Tolmachev YV, Sprunt S, Lopatina LM, Selinger JV (2007) Phys Rev E 76:061203
8. Yang ZP, Ci LJ, Bur JA, Lin SY, Ajayan PM (2008) Nano Lett 8:446
9. Sirbuly DJ, Law M, Pauzauskie P, Yan HQ, Maslov AV, Knutsen K, Ning CZ, Saykally RJ, Yang PD (2005) Proc Natl Acad Sci USA 102:7800
10. Shen YZ, Friend CS, Jiang Y, Jakubczyk D, Swiatkiewicz J, Prasad PN (2000) J Phys Chem B 104:7577
11. Bell AT (2003) Science 299:1688
12. Liu Q, Cui ZM, Ma Z, Bian SW, Song WG, Wan LJ (2007) Nanotechnology 18:385605
13. Lucas E, Decker S, Khaleel A, Seitz A, Fultz S, Ponce A, Li WF, Carnes C, Klabunde KJ (2001) Chemistry 7:2505
14. Xagas AP, Androulaki E, Hiskia A, Falaras P (1999) Thin Solid Films 357:173
15. Chan CK, Peng HL, Liu G, McIlwrath K, Zhang XF, Huggins RA, Cui Y (2008) Nat Nanotechnol 3:31
16. Kruis FE, Fissan H, Peled A (1998) J Aerosol Sci 29:511
17. Gratzel M (2001) Nature 414:338
18. Adams DM, Brus L, Chidsey CED, Creager S, Creutz C, Kagan CR, Kamat PV, Lieberman M, Lindsay S, Marcus RA, Metzger RM, Michel-Beyerle ME, Miller JR, Newton MD, Rolison DR, Sankey O, Schanze KS, Yardley J, Zhu XY (2003) J Phys Chem B 107:6668
19. Ostraat ML, Blauwe JWD, Green ML, Bell LD, Atwater HA, Flagan RC (2001) J Electrochem Soc 148:G265
20. Bjerneld EJ, Svendberg F, Kall M (2003) Nano Lett 3:593
21. Maynard AD, Kuempel ED (2005) J Nanopart Res 7:587
22. Maximova N, Dahl O (2006) Curr Opin Colloid Interf Sci 11:246
23. Kang M, Kim H, Han BW, Suh J, Park J, Choi M (2004) Microelectron Eng 71:229
24. Krinke TJ, Deppert K, Magnusson MH, Fissan H (2002) Part Part Syst Charact 19:321
25. Shenhar R, Rotello VM (2002) Acc Chem Res 36:549
26. Cimalla V, Stubenrauch M, Weise F, Fischer M, Tonisch K, Hoffmann M, Ambacher O (2007) Appl Phys Lett 90:101504
27. Klabunde KJ (2001) In: Klabunde KJ (ed) Nanoscale materials in chemistry. Wiley-Interscience, New York, p 1
28. Swihart MT (2003) Curr Opin Colloid Interf Sci 8:127
29. Kaiser N (2002) Appl Optics 41:3053
30. Hahn H (1997) Nanostruct Mater 9:3
31. Kennedy MK, Kruis FE, Fissan H, Mehta BR, Stappert S, Dumpich G (2003) J Appl Phys 93:551
32. Kato M (1976) Jpn J Appl Phys 15:757
33. Masanori T, Sawai S, Sengoku M, Kato M, Masumoto Y (2000) J Appl Phys 87:8535
34. El-Shall MS, Abdelsayed V, Pithawalla YN, Alsharach E, Deevi SC (2003) J Phys Chem B 107:2282
35. Ohno T (2002) J Nanopart Res 4:255
36. Bihari B, Eilers H, Tissue BM (1997) J Lumin 75:1
37. Krauss W, Birringer R (1997) Nanostruct Mater 9:109
38. Pithawalla YB, Deevi SC, El-Shall MS (2002) Mater Sci Eng A A329–A331:92
39. Jang HD, Friedlander SK (1998) Aerosol Sci Technol 29:81
40. Kim SY, Yu JH, Lee JS (1999) Nanostruct Mater 12:471
41. Han J, Chang H, Lee J, Chang H (2003) Aerosol Sci Technol 37:550
42. Sánchez-López JC, Justo A, Fernández A (1999) Langmuir 15:7822
43. Meakin P (1983) Phys Rev A 27:2616
44. Meakin P (1984) Phys Rev B Condens Matter 30:4207
45. Tassopoulos M, O'Brien JA, Rosner DE (1989) AIChE J 35:967
46. Krinke TJ, Deppert K, Magnusson MH, Schmidt F, Fissan H (2002) J Aerosol Sci 33:1341
47. Kulkarni P, Biswas P (2004) Aerosol Sci Technol 38:541
48. Kulkarni K, Biswas P (2003) J Nanopart Res 5:259
49. Gordon WO, Tissue BM, Morris JR (2007) J Phys Chem C 111:3233
50. Eilers H, Tissue BM (1995) Mater Lett 24:261
51. Tissue BM, Yuan HB (2003) J Solid State Chem 171:12
52. Levoska J, Tyunina M, Leppävuori S (1999) NanoStruct Mater 12:101
53. Pereira A, Cultrera L, Dima A, Susu M, Perrone A, Du HL, Volkov AO, Cutting R, Datta PK (2006) Thin Solid Films 497:142
54. Lao JY, Huang JY, Wang DZ, Ren ZF (2003) Nano Lett 3:235
55. Hawkeye MM, Brett MJ (2007) J Vac Sci Technol A 25:1317
56. Friedlander SK (2000) Smoke, dust, and haze: fundamentals of aerosol dynamics. Oxford University Press, New York
57. Lam HM, Hong MH, Yuan S, Chong TC (2004) Appl Phys A 79:2099
58. Pászti Z, Pet G, Horváth ZE, Karacs A (2000) Appl Surf Sci 168:114
59. Strobel R, Pratsinis SE (2007) J Mater Chem 17:4743
60. Dosev D, Guo B, Kennedy IM (2006) J Aerosol Sci 37:402
61. Katagiri S, Ishizawa N, Marumo F (1993) Powder Diffract 8:60
62. Vogt GJ (1988) Proc Electrochem Soc 88:572
63. Kaito C (1981) J Cryst Growth 55:273
64. Alayan R, Arnaud L, Broyer M, Cottancin E, Lerme J, Vialle JL, Pellarin M (2006) Phys Rev B 73:125444
65. Happy, Mohanty SR, Lee P, Tan TL, Springham SV, Patran A, Ramanujan RV, Rawat RS (2006) Appl Surf Sci 252:2806
66. Geohegan DB, Puretzky AS, Duscher G, Pennycook SJ (1998) Appl Phys Lett 72:2987
67. Nakata Y, Muramoto J, Okada T, Maeda M (2002) J Appl Phys 91:1640
68. Sánchez-López JC, Fernández A (2000) Acta Mater 48:3761
69. Yatsuya S, Yanagida A, Yamauchi K, Mihama K (1984) J Cryst Growth 70:536
70. Kaito C, Fujita K, Shiojiri M (1976) J Appl Phys 47:5161
71. Abdelsayed V, El-Shall MS (2007) J Chem Phys 126:024706
72. Furusawa H, Sakka T, Ogata YH (2004) J Appl Phys 96:975
73. Novopashin SA, Muriel A (1998) JETP Lett 68:582
74. Pfau P, Sattler K, Muhlbach J, Pflaum R, Recknagel E (1982) J Phys F Metal Phys 12:2131
75. Novopashin S, Muriel A (2002) J Exp Theoret Phys 95:262
76. Nanda KK, Kruis FE, Fissan H, Acet M (2002) J Appl Phys 91:2315